Article:

Angadi, V.C., Benz, F., Tischer, I. et al. (3 more authors) (2017) Evidence of terbium and oxygen co-segregation in annealed AlN:Tb. Applied Physics Letters, 110 (22). p. 222102. ISSN 0003-6951

https://doi.org/10.1063/1.4984237

The following article appeared in Appl. Phys. Lett. 110, 222102 (2017), and may be found at https://doi.org/10.1063/1.4984237).

Evidence of terbium and oxygen co-segregation in annealed AlN:Tb

V.C. Angadi,[1] F. Benz,[2] I. Tischer,[3,4] K. Thonke,[3] T. Aoki,[5] and T. Walther[1, a)]
[1)] *Dept. Electronic & Electrical Eng., Kroto Centre for High-Resolution Imaging and Spectroscopy, University of Sheffield, North Campus, Wheeldon Street, Sheffield S3 7HQ, UK*
[2)] *Institute of Materials Science, University of Stuttgart, Heisenbergstr 3, 70569 Stuttgart, Germany*
[3)] *Institut für Halbleiterphysik, Universität Ulm, D-89069 Ulm, Germany*
[4)] *now at: Richter lighting technologies GmbH, Böbinger Str. 34, 73540 Heubach, Germany*
[5)] *LeRoy Eyring Center for Solid State Science, Arizona State University, Tempe AZ 85287, USA*

(Dated: 5 May 2017)

Analytical scanning transmission electron microscopy (STEM) has been applied to study aluminium nitride (AlN) doped with terbium (Tb) and annealed at 800°C. Correlation of the maps of Tb and oxygen (O) from electron energy-loss spectrum (EELS) imaging proves that these two elements co-segregate, replacing aluminium (Al) and nitrogen (N) atoms, respectively. This agrees well with modelling which predicted the existence of Tb−O complexes needed to fit all lines in the rather complicated cathodoluminescence (CL) emission spectrum of the sample.

PACS numbers: 29.30.Dn, 42.70.Qs, 61.72.-y, 61.72.Cc, 61.72.J-, 61.72.sh, 61.72.uj, 64.75.Qr, 68.37.Ma, 71.15.-m, 71.55.Eq, 78.60.Hk, 79.20.Uv, 81.05.Ea, 81.15.Cd
Keywords: aluminium nitride, terbium, segregation, luminescence, electron microscopy

I. INTRODUCTION

In general rare-earth metal dopants[1,2] produce narrow optical emission lines almost insensitive to temperature. Hence, they find application in cathode ray tubes (CRTs), optical fibres, electroluminescence etc[3]. Tb is a very important rare-earth metal dopant in semiconductors and is used for green emission. A common application of Tb is tuning the green light component in incandescent lamps which give white light. Over the years there has been a lot of research on creating ultra-violet (UV) light emitting diodes (LEDs). In principle, AlN with a 6.2 eV bandgap should be able to give an emission at ∼200 nm, but there are difficulties to overcome to make such UV emitters commercially available. This large bandgap makes AlN an ideal matrix for rare-earth ions which typically have emission wavelengths much longer than 200 nm. AlN combines high thermal conductivity with low electrical conductivity, which makes it ideal for certain electronic applications, e.g. as heat sinks and substrates for devices with low leakage currents. The Tb−Tb ionic interactions in semiconductors can be exploited to tune the emission from green to blue[4]. While segregation of phosphorous (P) dopants in silicon can constitute a problem for electronic devices[5], segregation of rare-earth atoms in lanthanide doped semiconductors may be beneficial: Rutherford Back-Scattering (RBS) has been used to show that erbium (Er) ions in gallium arsenide (GaAs) occupy displaced tetrahedral interstitial sites[6,7], and there has been speculation about co-segregation with oxygen (O) and other impurities co-doping of which is known to enhance the luminescence intensity in Si[8], GaAs[7] and AlN[9]. For Er & O co-doped (Al)GaAs a structural model of the defect consisting of one Er^{3+} and two O^{2-} ions with C_{2V} symmetry has been suggested based on the number of emission lines observed[6], but no direct evidence could be put forward, and such complexes would need further vacancies to remain electrically neutral. While europium (Eu) doped anatase[10] and Eu doped magnesia[11] show series of strong luminescence lines in the range of 550−720 nm, Tb doped alumina[12] and Tb doped but otherwise pure AlN[13] both display similar emission triplets at around 490 nm and 540 nm. This differs from the seven emission lines in CL we observe for Tb doped and annealed AlN where we directly observe Tb & O co-segregation by STEM. The segregation of Tb in AlN and the local cluster arrangements can be studied and observed by spectroscopy methods like CL and EELS. The possible formation of Tb complexes in Tb doped AlN has been conjectured based on CL[14]. The concentration of Tb in our AlN sample is ∼2 at.% as estimated by inductive coupled plasma - optical emission spectroscopy (ICP-OES) and energy dispersive X-ray spectroscopy (EDXS). A high resolution analytical STEM is needed to confirm directly segregation of single atoms into small complexes.

II. EXPERIMENTAL DETAILS

A. AlN:Tb sputter deposition

The AlN:Tb films were prepared by reactive direct current (DC) magnetron sputtering on silicon (Si) (100), which was used as received. Two Al targets (150 W each) and one Tb target (14 W) were used. As a sputtering atmosphere served a mixture of 75% N and 25% argon with a total pressure of 6×10^{-3} mbar. After the sputtering the films were annealed at 800°C for 30 min under a 1 bar N

[a)]e-mail: t.walther@sheffield.ac.uk

atmosphere to avoid decomposition. The annealing step is required to 'activate' the Tb luminescence - the intensity increases by a factor of approximately 25 during this treatment.

B. Cathodoluminescence details

We have performed CL spectroscopy in order to observe the characteristic Tb^{3+} luminescence. The narrow line-width of the Tb^{3+} emission at 9 K allowed us to examine splitting into a number of sub-levels depending on the coordination symmetry of Tb^{3+} (crystal field splitting). To do so we have used a Zeiss LEO DSM 982 SEM[15] (acceleration voltage: 7 kV, working distance: 4 mm) equipped with a helium-cooled cryostat. The emitted light was collected using a glass fibre which was placed on the sample. The light was analysed with a Spex monochromator (1200 l/mm grating, 250 mm blaze wavelength) and a liquid nitrogen cooled, back-illuminated UV optimized Jobin Yvon charge-coupled device (CCD).

C. STEM

Cross-sectional specimens were prepared using standard methods of cutting and gluing face-to-face two samples, grinding, polishing and low-energy argon ion milling until perforation near the centre. While thin amorphous layers may form on the specimen surfaces, structural disorder and oxidation of the surfaces may offset slightly the absolute values of but not alter significantly the cross-correlation between elemental maps. The STEM experiments were carried out using a Nion UltraSTEM 100 equipped with a Nion HERMES monochromator, aberration corrector and Gatan Enfinium ER spectrometer for EELS[16,17]. The microscope was operated at 60kV with 30 mrad beam convergence semi-angle. No energy-selecting slit in the dispersive plane of the monochromator was used, providing 0.12 nm probe size (nominal spot size of 20i), with ~300 pA beam current at an energy resolution better than 0.35 eV, as given by the characteristics of the cold field emitter electron gun. The collection semi-angle was >90 mrad for high-angle annular dark field (HAADF) imaging and <45 mrad with 3 mm entrance aperture for EELS. Spectra were acquired with the CCD detector in single read-out, vertical integration mode and a binning factor of 2 for fast acquisition to avoid electron beam-induced damage of the sample. This gave an effective energy dispersion of 0.7 eV/channel where the apparent width of the zero-loss peak was limited by the detector point spread function rather than the actual energy spread of the electrons. The acquisition parameters of two EELS SI are listed in Table I.

III. MODELLING

To further investigate the surroundings of Tb^{3+} ions, we have performed simulations of an AlN supercell (consisting of 18 actual AlN unit cells) using the MOPAC2012 software[18] with the extension SPARKLE[19] to describe the rare-earth ion. For pure, undoped AlN we found good agreement between the lattice constants of AlN predicted by our simulation (a = 3.12 Å; c = 5.05 Å) and previous reports (a = 3.11 Å; c = 4.98 Å)[20]. Subsequently, we have replaced an Al^{3+} ion with a Tb^{3+} one, three N^{3-} by O^{2-}, and another Al^{3+} by a vacancy to ensure charge neutrality. Initially we distributed these lattice defects within the supercell so that they were spaced far apart as in Fig. 1a and calculated the energy of formation of this 'random' state as our reference energy. We systematically varied the local arrangement, optimised the geometry, and compared the resulting energies of formation. We find that placing the O ions in the nearest neighbouring positions of the Tb ion leads to an energy increase of around 2.5 eV per supercell. In contrast, if the Al vacancy V_{Al} is placed next to the Tb ion we find that the energy of formation is reduced by -1.38 eV. This reduction is likely due to the release of strain energy which is introduced by the larger atomic radius of the Tb^{3+} ion compared to the Al^{3+} one. Gradually coordinating the Al vacancy with more and more O anions leads to a further degrease in energy (-4.98 eV). The geometry of this hypothetical lowest energy state is shown in Fig. 1b. We denote these complexes according to the coordination of the vacancy, for instance the lowest energy one as $(V_{Al})(O)_3(NTb)$. Fig. 1c shows an overview of the energies of different $V_{Al}-N-Tb$ complexes considered. Probably these complexes are formed during the annealing procedure, which is necessary to 'activate' the rare-earth luminescence. From the fully relaxed structure we find a reduction of the local symmetry of the Tb^{3+} lattice site from T_d to C_{3v}, corresponding to a slight change in the bond length along one direction of the coordination tetrahedron. To verify this reduction in symmetry we have recorded CL spectra of the $^5D_4$ to $^7F_5$ transition of the trivalent Tb ions at 9 K (see Fig. 1d). This transition reveals a seven-fold splitting of the $^7F_5$ energy level, which is consistent with the expected number of states in the case of the C_{3v} symmetry (for T_d only four states would be expected)[21]. At room temperature, thermal broadening of the lines occurs and their emission intensity decreases, yielding more noise, however, the position of the most intense lines in the 2.2-2.3 eV range remains unaltered from which we conclude the crystal symmetry does not change at higher temperature.

TABLE I. EELS data acquisition parameters for the two spectrum images (SI) acquired from the same area at 60kV.

Attributes	Low loss SI	High loss SI
Spatial image size (pixels)	87×100	87×100
Spectrum channels	2048	512
Dispersion (eV per channel)	0.7	2.8
Field of view height (nm)	70	70
Conv. semi-angle (α)(mrad)	30	30
Coll. semi-angle (β)(mrad)	45	45
Spectrum offset (eV)	0	310
Exposure time (seconds)	8×10^{-5}	1×10^{-1}
Total acquisition time	~ 700 ms	~ 14 min 30 s

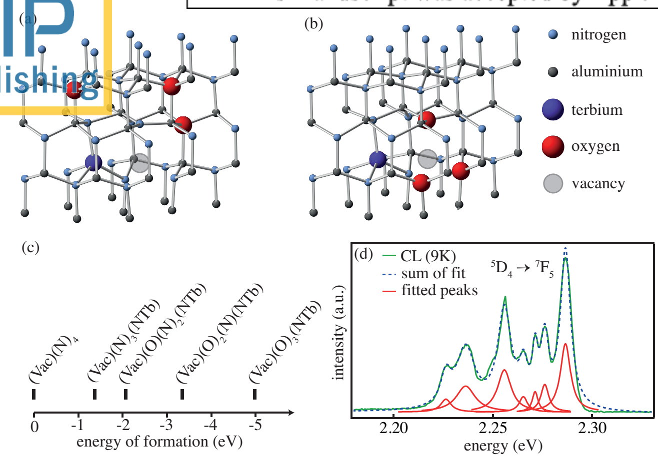

FIG. 1. Illustration of the models of the vacancy/Tb^{3+} complex with (a) no (b) three oxygen atoms attached to it. (c) Comparison of the energies of formation of different $Tb-N-V_{Al}$ complexes. The names show the four nearest neighbours of the Al vacancy. (d) High resolution CL spectrum of the $^5D_4$ to $^7F_5$ transition of Tb^{3+} ions incorporated in AlN.

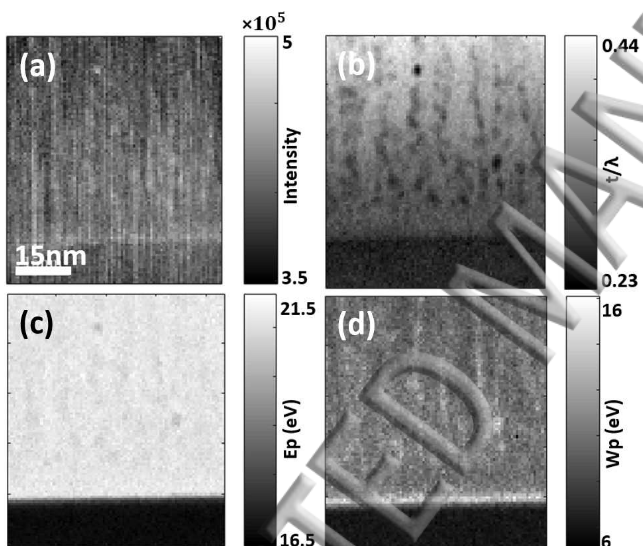

FIG. 2. (a) HAADF and maps of (b) relative thickness, (c) plasmon peak energy, (d) plasmon width.

IV. STEM EELS SI

All acquired SI have a field of view of 70 nm and have been rotated through $\sim 90°$ so that the growth direction in all maps points upwards (AlN on top of Si). A HAADF image is shown in Fig. 2a. The vertical lines in the HAADF image are artefacts due to emission current fluctuations of the cold field emitter electron gun. A relative thickness map is shown in Fig. 2b. The inelastic mean free path (λ) values in Si (substrate), AlN:Tb region and SiO_2 region at 60 kV are $\approx$49 nm, $\approx$52 nm and $\approx$54 nm, respectively[22]. The values of the relative thickness (t/λ) map can thus be directly related to absolute specimen thickness (t) in the range of 13−20 nm. For calculation of t/λ, the intensity of the spectra up to the minimum between zero-loss peak and plasmon peak is approximated as the intensity of the zero-loss (I_0). Hence I_0 contains not only zero-loss intensity, but also phonon losses, some retardation and Čerenkov losses etc. The total intensity (I_t) also contains inter-band transitions, plasmon losses and ionization core-losses. Hence the t/λ values calculated from eqn. 1 will always be slightly overestimated (giving a mean of $\overline{t/\lambda} = 0.32$ over the whole range in Fig.2b).

TABLE II. Calculated mean free paths (λ).

Composition at.%	Al:N:Tb:O 48 : 49 : 2 : 1	Si:O 33.3 : 66.7	Si:O 99 : 1
$\langle Z \rangle$	11.05	10.00	13.94
$\langle A \rangle$	23.15	20.03	27.97
$\langle E \rangle$ [eV]	18.0	17.4	19.6
λ [nm]	52.4	54.0	48.9

$$t/\lambda = \ln\left(\frac{I_t}{I_0}\right) \tag{1}$$

More accurate ways to measure t/λ would include fitting the bulk plasmon with a Lorentz function $L(E, E_p, W_p)$ (eqn. 3) and the monochromated zero-loss with a Gaussian function $G(E, E_0, W_0)$ (eqn. 4) and weighting both according to a Poisson distribution $P(n, t/\lambda)$ simultaneously, as shown in eqns. 2 & 5.

$$P(n, t/\lambda) = \left(\frac{t}{\lambda}\right)^n \left(\frac{1}{n!}\right) \exp\left(-\frac{t}{\lambda}\right) \tag{2}$$

$$L(E, E_p, W_p) = \frac{A_p}{\pi} \frac{\frac{1}{2}W_p}{(E - E_p)^2 + \left(\frac{1}{2}W_p\right)^2} \tag{3}$$

$$G(E, E_0, W_0) = \frac{0.939A_0}{W_0} \exp\left(-\frac{(E - E_0)^2}{0.36W_0^2}\right) \tag{4}$$

$$\begin{aligned} S(E, t/\lambda, E_0, W_0, E_p, W_p) &= P(0, t/\lambda)\ G(E, E_0, W_0) \\ &+ \sum_{k=1}^{n} P(k, t/\lambda)\ L(E, k \times E_p, W_p) \end{aligned} \tag{5}$$

where $n = \lfloor E_{max}/E_p \rfloor \in \mathbb{N}$ is the integer number of plasmon losses considered. t/λ, position (E_0) and full width at half maximum (FWHM) (W_0) of the zero-loss peak, position (E_p) and FWHM (W_p) of bulk plasmon are the fitting parameters. Eqn. 1 can be used as an initial estimate of t/λ in multiple linear least-squares (MLLS) fitting of the low loss in eqn. 5. This can be extended to the entire SI, which provides more accurate t/λ values ($\overline{t/\lambda}$ =0.31, $\overline{R^2}$ =0.992). Figs. 2c & 2d are maps of E_p and W_p obtained from eqn. 3 where the values of the plasmon peak energy have been interpolated to sub-pixel precision ($\approx$0.1 eV). The FWHM (W_p) of bulk plasmons (Fig. 2d) of oxides are known to be wider than those of compound semiconductors. Elemental maps are shown in Figs. 3a-3e. The background fitting details are listed in Table III along with the integration ranges (Δ). The

TABLE III. Background fitting details. All numerical values are in eV.

SI	edge	fit begin	fit end	onset	Δ	fit type
low loss	Al $L_{2,3}$	23.8	70	72.8	27.3	Exp2[a]
	Si $L_{2,3}$	41.3	98	99.4	105	Exp2
high loss	N K	343.6	385.6	385.6	112	Pow[b]
	O K	427.6	517.2	525.6	112	Exp1[c]
	Tb $M_{4,5}$	727.2	1147.2	1211.6	246.4	Exp1

[a] Superposition of two exponential decay functions (eqn. 6).
[b] Inverse power-law function (eqn. 7).
[c] Exponential decay function (eqn. 6).

TABLE IV. Elemental quantification (at.%) in AlN:Tb and Si region for top 40 rows (A) and lowest 15 rows (B) respectively.

Box	Region	Al	N	Tb	O	Si
A	AlN:Tb	43.2	38.7	1.4	15.8	0.01
B	Si	17.2	0	0.8	20.3	62.3

functions used to fit the background are exponential decay (eqn. 6) or inverse power-law functions (eqn. 7).

$$f(E) = \sum_{j=1}^{j=k} \begin{bmatrix} A_1 \\ \cdot \\ \cdot \\ A_j \end{bmatrix} \exp\left(- \begin{bmatrix} r_1 \\ \cdot \\ \cdot \\ r_j \end{bmatrix} E \right) \tag{6}$$

$$f(E) = AE^{-r} \tag{7}$$

The value of k =1 for fit type 'Exp1', and k =2 for fit types 'Exp2' and 'Pow' as indicated in Table III. The Si $L_{2,3}$ edge and Al $L_{2,3}$ core-losses are extracted from low loss SI. N K, O K and Tb $M_{4,5}$ edges are extracted from high loss SI. The integration range (Δ) for Al $L_{2,3}$ is limited by overlap with the Si $L_{2,3}$ edge. The maps of Al $L_{2,3}$ and Si $L_{2,3}$ (Figs. 3a & 3b) are relatively noisy due to the low exposure time and hence low signal-to-noise ratio (SNR). Large negative values in the Si $L_{2,3}$ map are due to poor background fitting in the AlN region due to the preceding Al $L_{2,3}$ ionization edge. Deconvolution is not applied because of the low SNR in the spectrum: deconvolution by Fourier-ratio or Richardson-Lucy methods would increase the noise even further. The interface in the high loss maps (Figs. 3c-3e) appears to be inclined with respect to the horizontal by an angle of ≈4.6° due to drift during the long time of acquisition. Due to this mismatch in the interface, the at.% values have been calculated only in the regions indicated in Fig. 3f. The apparent SiO_2 layer widths in Figs. 2d & 3d differ by 3.5 nm due to slight drift between low and high loss region SIs, but this does not prevent direct comparison of Figs. 3c-3e.

V. DISCUSSION

In case of N K and O K (Figs. 3c & 3d), the contrast of the maps indicates anti-correlation, i.e. in the AlN region, O is replacing N (group V sub-lattice). Tb must

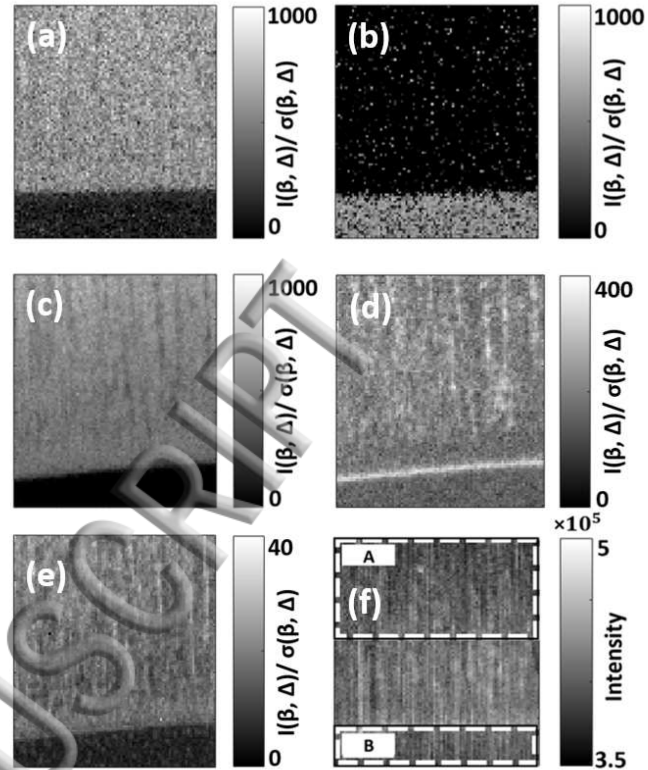

FIG. 3. Background subtracted net intensities after the edge onsets have been integrated and normalised with respect to the corresponding scattering cross-sections and exposure times. Elemental maps of Al $L_{2,3}$ (a) and Si $L_{2,3}$ (b) in the low loss region. Elemental maps of N K (c), O K (d) and Tb $M_{4,5}$ (e) in the high loss region. (f) Box A area in AlN used for the calculation of cross-correlation between elemental maps. Region B includes the Si substrate.

be replacing Al in the group III sub-lattice, although the corresponding decrease in local Al contrast is too small to be clearly visible in Fig. 3a. Table V lists the cross-correlation values (X_{corr}) between the elemental maps in the top half of AlN marked in Fig. 3f, calculated using MATLAB function `corr2(x,y)`, where x and y are the elemental maps from Figs. 3a-3e at region A marked in Fig. 3f. The cross-correlation of N and Tb map is negative. Similar observations can be made between N and O. The cross-correlation between Tb and O maps is positive, indicating the formation of Tb−O complexes. In conclusion, the STEM analysis demonstrates co-segregation of the Tb ions together with O ions (which are a common impurity of AlN) in AlN. These experimental results are consistent with atomistic simulations in Fig 1b.

TABLE V. Cross-correlation between elemental maps in AlN region marked by box in Fig. 3f.

X_{corr}	Al	N	Tb	O	Si
Al	1.0000	0.0802	0.0337	0.0012	−0.0920
N	0.0802	1.0000	**−0.0366**	**−0.3694**	−0.0060
Tb	0.0337	−0.0366	1.0000	**0.3466**	0.0064
O	0.0012	−0.3694	0.3466	1.0000	0.0188
Si	−0.0920	−0.0060	0.0064	0.0188	1.0000

ACKNOWLEDGMENTS

We gratefully acknowledge the use of facilities within the LeRoy Eyring Center for Solid State Science at Arizona State University. FB acknowledges the long-standing guidance and help of Prof. Dr. H. P. Strunk who passed away on 17$^{\text{th}}$ of August 2015.

[1] A. J. Kenyon, Current Opinion in Sol. St. and Mater. Sci. **7**, 143 (2003).

[2] A. J. Kenyon, Progress in Quantum Electronics **26**, 225 (2002).

[3] T. Aitasalo, P. Dereń, J. Hölsä, H. Jungner, J.-C. Krupa, M. Lastusaari, J. Legendziewicz, J. Niittykoski, and W. Stręk, J. Sol. State Chem. **171**, 114 (2003).

[4] F. Benz, H. P. Strunk, J. Schaab, U. Künecke, and P. Wellmann, J. Appl. Phys. **114**, 073518 (2013).

[5] J. G. Keizer, S. R. McKibbin, and M. Y. Simmons, ACS nano **9**, 7080 (2015).

[6] K. Takahei, A. Taguchi, Y. Horikoshi, and J. Nakata, J. Appl. Phys. **76**, 4332 (1994).

[7] J. M. Zavada and D. Zhang, Sol. State Electron. **38**, 1285 (1995).

[8] J. Michel, J. L. Benton, R. F. Ferrante, D. C. Jacobson, D. J. Eaglesham, E. A. Fitzgerald, Y. H. Xie, J. M. Poate, and L. C. Kimerling, J. Appl. Phys. **70**, 2672 (1991).

[9] J. C. Oliveira, A. Cavaleiro, M. T. Vieira, L. Bigot, C. Garapon, J. Mugnier, and B. Jacquier, Thin Solid Films **446**, 264 (2004).

[10] M. Pal, U. Pal, J. M. G. Y. Jiménez, and F. Pérez-Rodríguez, Nanoscale Res. Lett. **7**, 1 (2012).

[11] C. K. Rastogi, S. Saha, S. Sivakumar, and G. S. Pala, Phys. Chem. Chem. Phys. **17**, 4600 (2015).

[12] E. H. Penilla, Y. Kodera, and J. E. Garay, Adv. Func. Mat. **23**, 6036 (2013).

[13] A. T. Wieg, Y. Kodera, Z. Wang, T. Imai, C. Dames, and J. E. Garay, Appl. Phys. Lett. **101**, 111903 (2012).

[14] F. Benz, T. Walther, and H. P. Strunk, J. Phys. Conf. Ser. **471**, 012032 (2013).

[15] M. Schirra, A. Reiser, G. M. Prinz, A. Ladenburger, K. Thonke, and R. Sauer, J. Appl. Phys. **101**, 113509 (2007).

[16] O. L. Krivanek, T. C. Lovejoy, N. Dellby, and R. W. Carpenter, *J. Electron Microsc.*, **62**, 3 (2013).

[17] O. L. Krivanek, T. C. Lovejoy, and N. Dellby, J. Microsc. **259**, 165 (2015).

[18] J. J. Steward, *MOPAC2012*, Steward Computation Chemistry (2012), http://openmopac.net/.

[19] R. O. Freire and A. M. Simas, J. Chem. Theory and Computation **6**, 2019 (2010).

[20] Intern. Centre for Diffraction Data (ICDD) (2011), 00-025-1133.

[21] B. Henderson and R. H. Bartram, *Crystal-Field Engineering of Solid-State Laser Materials*, Vol. 25 (Cambridge Univ. Press, 2005).

[22] R. F. Egerton, *Electron Energy-Loss Spectroscopy in the Electron Microscope*, 3rd ed. (Springer, New York, 2011).

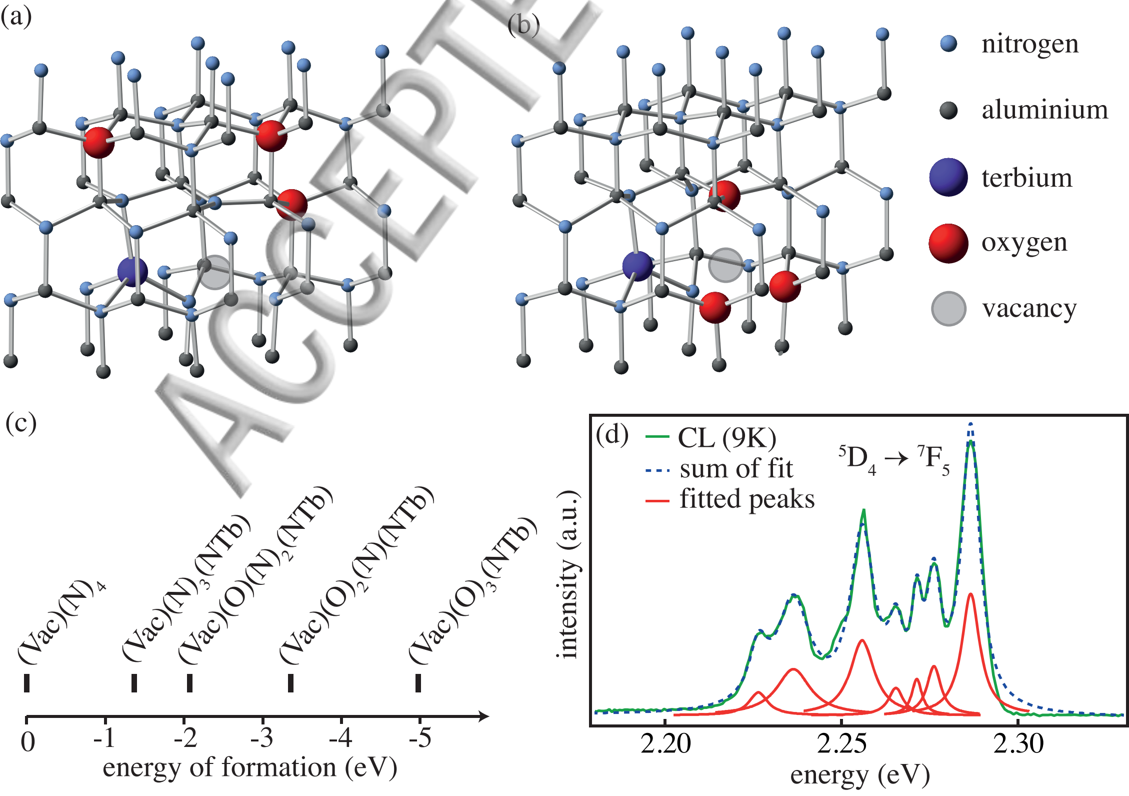

(a)
(b)
nitrogen
aluminium
terbium
oxygen
vacancy
(c)
(Vac)(N)$_4$
(Vac)(N)$_3$(NTb)
(Vac)(O)(N)$_2$(NTb)
(Vac)(O)$_2$(N)(NTb)
(Vac)(O)$_3$(NTb)
0
-1
-2
-3
-4
-5
energy of formation (eV)
(d)
CL (9K)
sum of fit
fitted peaks
$^5D_4 \rightarrow {}^7F_5$
intensity (a.u.)
2.20
2.25
2.30
energy (eV)

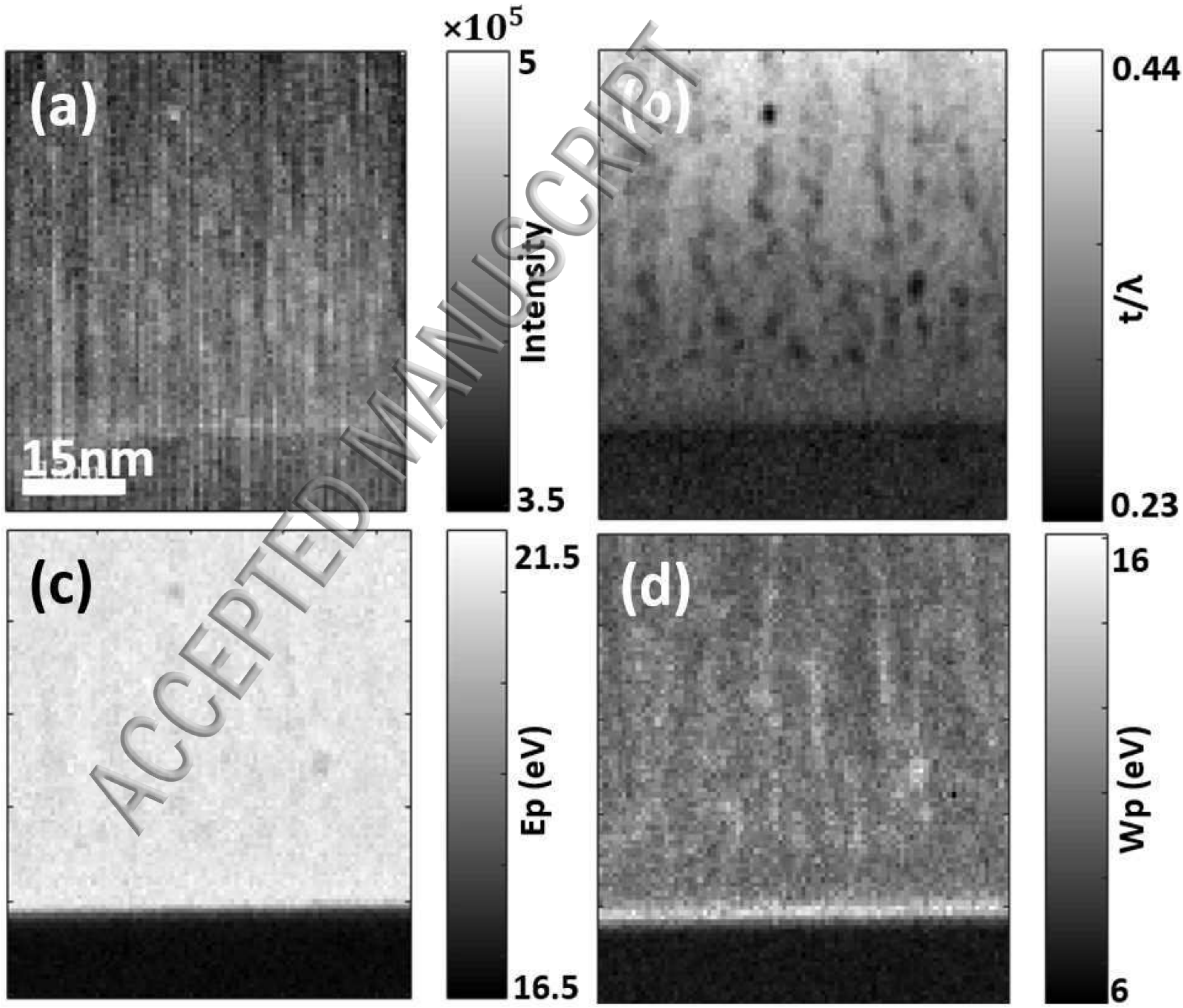
×10^5
5
3.5
Intensity
(a)
15nm
(b)
0.44
0.23
t/λ
(c)
21.5
16.5
Ep (eV)
(d)
16
6
Wp (eV)

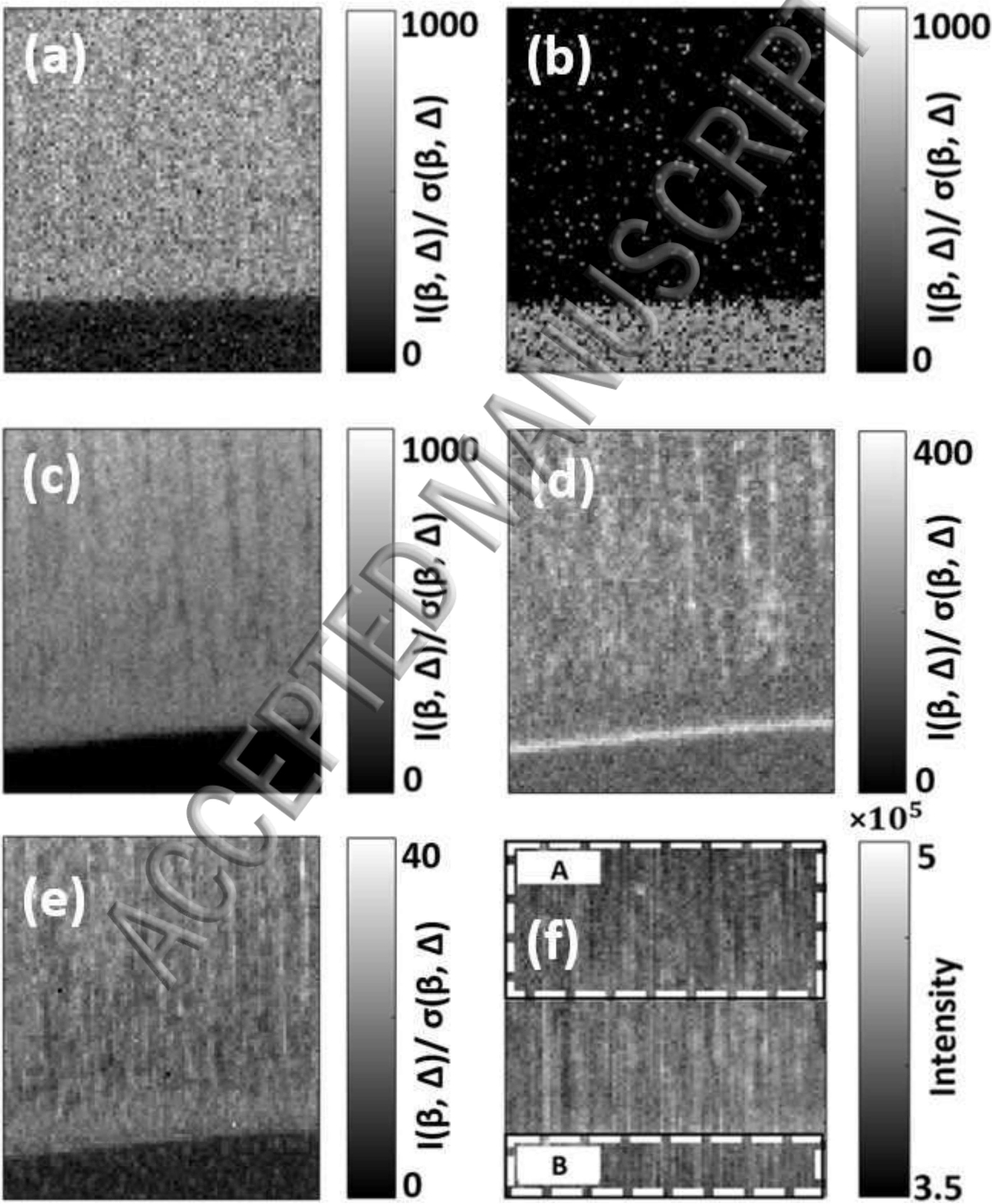

(a)
1000
0
I(β, Δ)/ σ(β, Δ)
(b)
1000
0
I(β, Δ)/ σ(β, Δ)
(c)
1000
0
I(β, Δ)/ σ(β, Δ)
(d)
400
0
I(β, Δ)/ σ(β, Δ)
(e)
40
0
I(β, Δ)/ σ(β, Δ)
(f)
A
B
×10^5
5
3.5
Intensity